Commun. Comput. Phys.
doi: 10.4208/cicp.311009.081110s

Vol. **9**, No. 5, pp. 1206-1218
May 2011

Lattice Boltzmann Simulations of Water Transport from the Gas Diffusion Layer to the Gas Channel in PEFC

Koji Moriyama[1,2,*] and Takaji Inamuro[2,3]

[1] *Fundamental Research Center, Honda R&D Co. Ltd., Saitama 351-0193, Japan.*
[2] *Department of Aeronautics and Astronautics, Graduate School of Engineering, Kyoto University, Kyoto 606-8501, Japan.*
[3] *Advanced Research Institute of Fluid Science and Engineering, Graduate School of Engineering, Kyoto University, Kyoto 606-8501, Japan.*

Received 31 October 2009; Accepted (in revised version) 8 November 2010

Available online 28 January 2011

Abstract. Water management is a key to ensuring high performance and durability of polymer electrolyte fuel cell (PEFC), and it is important to understand the behavior of liquid water in PEFC. In this study, the two-phase lattice Boltzmann method is applied to the simulations of water discharge from gas diffusion layers (GDL) to gas channels. The GDL is porous media composed of carbon fibers with hydrophobic treatment, and the gas channels are hydrophilic micro-scale ducts. In the simulations, arbitrarily generated porous materials are used as the structures of the GDL. We investigate the effects of solid surface wettabilities on water distribution in the gas channels and the GDL. Moreover, the results of *X*-ray computed tomography images in the operating PEFC are compared with the numerical simulations, and the mechanism of the water transport in PEFC is considered.

AMS subject classifications: 76M28, 76T10, 76S05, 65D18

Key words: Two-phase lattice Boltzmann method, polymer electrolyte fuel cell, *X*-ray CT imaging, gas diffusion layer.

1 Introduction

Polymer electrolyte fuel cell (PEFC) is expected to be the future driving power of vehicles because of its low emission and high efficient conversion into energy. The PEFC is composed of an electrolyte membrane, a catalyst layer, a gas diffusion layer (GDL), bipolar plates, etc. Water management in the PEFC is one of the inevitable and difficult issues to

*Corresponding author. *Email addresses:* koji_moriyama@n.t.rd.honda.co.jp (K. Moriyama), inamuro@kuaero.kyoto-u.ac.jp (T. Inamuro)

realize high performance and durability. While the electrolyte membrane has to be kept humid to facilitate proton conductivity, the liquid water in the catalyst layer, GDL and gas channels has to be continually discharged to ensure oxygen or hydrogen transport to catalyst surfaces [1].

Recently, various investigations of water transport in the GDL and the gas channels have been performed [2–5]. However, they are elementary evaluations of the GDL and the gas channels, and there are few pore-scale analyses on water transport in the GDL and the gas channels at the same time. Furthermore, there are few studies which compare in-situ measurements in the operating PEFC to numerical simulations with the complex GDL geometries.

In this study, in order to obtain fundamental knowledge of water transport in the PEFC, two-phase lattice Boltzmann simulations are performed and compared with *X*-ray computed tomography images in the operating PEFC. In the simulations, the surface tension of liquid water, the wettability of the GDL and the gas channel, and the high density and viscosity ratios of water and air are taken into account.

The paper is organized as follows. In Section 2, we describe the numerical method and the computational setup. Comparison with *X*-ray computed tomography images and numerical results are shown in Section 3. Finally, conclusions are given in Section 4.

2 Numerical method and calculation conditions

2.1 Two-phase lattice Boltzmann method

Recently, the lattice Boltzmann method has been developed into an alternative and promising numerical scheme for simulating viscous fluid flows and multi-phase fluid flows. The advantages of the lattice Boltzmann method are the simplicity of the algorithm, the accuracy of the mass and momentum conservations, the straightforward resolution of complex boundaries, and the suitability for parallel computing. These features are quite suitable for simulating multiphase flows in the complex GDL.

In this study, the two-phase lattice Boltzmann method proposed by Inamuro et al. [6], which can simulate two-phase flows with a large density ratio, is used. The fifteen-velocity model ($N=15$) is used in the present paper. The velocity vectors in this model are given by

$$\begin{aligned}&\left[\boldsymbol{c}_1,\boldsymbol{c}_2,\boldsymbol{c}_3,\boldsymbol{c}_4,\boldsymbol{c}_5,\boldsymbol{c}_6,\boldsymbol{c}_7,\boldsymbol{c}_8,\boldsymbol{c}_9,\boldsymbol{c}_{10},\boldsymbol{c}_{11},\boldsymbol{c}_{12},\boldsymbol{c}_{13},\boldsymbol{c}_{14},\boldsymbol{c}_{15}\right]\\ &=\begin{bmatrix} 0 & 1 & 0 & 0 & -1 & 0 & 0 & 1 & -1 & 1 & 1 & -1 & 1 & -1 & -1\\ 0 & 0 & 1 & 0 & 0 & -1 & 0 & 1 & 1 & -1 & 1 & -1 & -1 & 1 & -1\\ 0 & 0 & 0 & 1 & 0 & 0 & -1 & 1 & 1 & 1 & -1 & -1 & -1 & -1 & 1 \end{bmatrix}. \end{aligned} \tag{2.1}$$

Two particle velocity distribution functions, f_i and g_i are used. The function f_i is used for the calculation of an order parameter which represents two phases, and the function g_i is used for the calculation of a predicted velocity of the two-phase fluid without a

pressure gradient. The evolution of the particle distribution functions $f_i(\boldsymbol{x},t)$ and $g_i(\boldsymbol{x},t)$ with velocity $\boldsymbol{c}_i$ at the lattice point $\boldsymbol{x}$ and at time t is computed by

$$f_i(\boldsymbol{x}+\boldsymbol{c}_i\Delta x,t+\Delta t)=f_i^{\rm c}(\boldsymbol{x},t), \tag{2.2}$$

$$g_i(\boldsymbol{x}+\boldsymbol{c}_i\Delta x,t+\Delta t)=g_i^{\rm c}(\boldsymbol{x},t), \tag{2.3}$$

where $f_i^{\rm c}$ and $g_i^{\rm c}$ are functions of Chapman-Enskog type in which variables $\boldsymbol{x}$ and t enter only through macroscopic variables and/or their derivatives. The order parameter ϕ distinguishing the two phases and the predicted velocity $\boldsymbol{u}^*$ of the multicomponent fluids are defined in terms of the two particle velocity distribution functions

$$\phi=\sum_{i=1}^{15} f_i, \tag{2.4}$$

$$\boldsymbol{u}^*=\sum_{i=1}^{15} g_i\boldsymbol{c}_i. \tag{2.5}$$

The functions $f_i^{\rm c}$ and $g_i^{\rm c}$ in Eqs. (2.2) and (2.3) are given by

$$f_i^{\rm c}=H_i\phi+F_i\Big[p_0-\kappa_f\phi\nabla^2\phi-\frac{\kappa_f}{6}|\nabla\phi|^2\Big]+3E_i\phi c_{i\alpha}u_\alpha+E_i\kappa_f G_{\alpha\beta}(\phi)c_{i\alpha}c_{i\beta}, \tag{2.6}$$

$$\begin{aligned} g_i^{\rm c}=E_i\Big\{&1+3c_{i\alpha}u_\alpha-\frac{3}{2}u_\alpha u_\alpha+\frac{9}{2}c_{i\alpha}c_{i\beta}u_\alpha u_\beta+\frac{3}{4}\Delta x\Big(\frac{\partial u_\beta}{\partial x_\alpha}+\frac{\partial u_\alpha}{\partial x_\beta}\Big)c_{i\alpha}c_{i\beta}\\ &+3c_{i\alpha}\frac{1}{\rho}\frac{\partial}{\partial x_\beta}\Big[\mu\Big(\frac{\partial u_\beta}{\partial x_\alpha}+\frac{\partial u_\alpha}{\partial x_\beta}\Big)\Big]\Delta x\Big\}+E_i\frac{\kappa_g}{\rho}G_{\alpha\beta}(\rho)c_{i\alpha}c_{i\beta}-\frac{2}{3}F_i\frac{\kappa_g}{\rho}|\nabla\rho|^2, \end{aligned} \tag{2.7}$$

where

$$H_1=1, \qquad H_2=H_3=\cdots=H_{15}=0, \tag{2.8a}$$

$$F_1=-\frac{7}{3}, \qquad F_i=3E_i \ \ (i=2,3,\cdots,15), \tag{2.8b}$$

and

$$G_{\alpha\beta}(\phi)=\frac{9}{2}\frac{\partial\phi}{\partial x_\alpha}\frac{\partial\phi}{\partial x_\beta}-\frac{3}{2}\frac{\partial\phi}{\partial x_\gamma}\frac{\partial\phi}{\partial x_\gamma}\delta_{\alpha\beta}, \tag{2.9}$$

with $\alpha,\beta,\gamma=x,y,z$. In the above equations, $\delta_{\alpha\beta}$ is the Kronecker delta, κ_f is a constant parameter determining the width of the interface, κ_g is a constant parameter determining the strength of the surface tension, and the other variables, ρ, $\rho_{\rm L}$, μ, and $\boldsymbol{u}$ are defined below. In Eq. (2.6), p_0 is given by

$$p_0=\phi T_\phi\frac{1}{1-b\phi}-a\phi^2, \tag{2.10}$$

where a,b, and T_ϕ are free parameters determining the maximum and minimum values of ϕ. The density in the interface is obtained by using the cut-off values of the order parameter, $\phi_{\rm L}^*$ and $\phi_{\rm G}^*$, for the liquid and gas phases with the following relation:

$$\rho=\begin{cases}\rho_{\rm G}, & \phi<\phi_{\rm G}^*,\\ \frac{\Delta\rho}{2}\left[\sin\left(\frac{\phi-\overline{\phi^*}}{\Delta\phi^*}\pi\right)+1\right]+\rho_{\rm G}, & \phi_{\rm G}^*\le\phi\le\phi_{\rm L}^*,\\ \rho_{\rm L}, & \phi>\phi_{\rm L}^*,\end{cases} \tag{2.11}$$

where $\rho_{\rm G}$ and $\rho_{\rm L}$ are the density of gas and liquid phase, respectively, $\Delta\rho=\rho_{\rm L}-\rho_{\rm G}$, $\Delta\phi^*=\phi_{\rm L}^*-\phi_{\rm G}^*$, and $\overline{\phi^*}=(\phi_{\rm L}^*+\phi_{\rm G}^*)/2$. The viscosity μ in the interface is obtained by

$$\mu=\frac{\rho-\rho_{\rm G}}{\rho_{\rm L}-\rho_{\rm G}}(\mu_{\rm L}-\mu_{\rm G})+\mu_{\rm G}, \tag{2.12}$$

where $\mu_{\rm G}$ and $\mu_{\rm L}$ are the viscosity of gas and liquid phase, respectively, and both are of $\mathcal{O}(\Delta x)$. Since $\boldsymbol{u}^*$ is not divergence free ($\nabla\cdot\boldsymbol{u}^*\neq0$) in general, a correction of $\boldsymbol{u}^*$ is required. The current velocity $\boldsymbol{u}$ which satisfies the continuity equation ($\nabla\cdot\boldsymbol{u}=0$) can be obtained by using

$$\mathrm{Sh}\frac{\boldsymbol{u}-\boldsymbol{u}^*}{\Delta t}=-\frac{\nabla p}{\rho}, \tag{2.13}$$

$$\nabla\cdot\left(\frac{\nabla p}{\rho}\right)=\mathrm{Sh}\frac{\nabla\cdot\boldsymbol{u}^*}{\Delta t}, \tag{2.14}$$

where $\mathrm{Sh}=U/c$ is the Strouhal number and p is the pressure. The Poisson equation (2.14) can be solved by various methods. In the present paper, we solve it in the framework of LBM. Namely, the following evolution equation of the velocity distribution function h_i is used for the calculation of the pressure p:

$$h_i^{n+1}(\boldsymbol{x}+\boldsymbol{c}_i\Delta x)=h_i^n(\boldsymbol{x})-\frac{1}{\tau_h}\left[h_i^n(\boldsymbol{x})-E_ip^n(\boldsymbol{x})\right]-\frac{1}{3}E_i\frac{\partial u_\alpha^*}{\partial x_\alpha}\Delta x, \tag{2.15}$$

where n is the number of iterations and the relaxation time τ_h is given by

$$\tau_h=\frac{1}{\rho}+\frac{1}{2}. \tag{2.16}$$

The pressure is obtained by

$$p=\sum_{i=1}^{15}h_i. \tag{2.17}$$

The iteration of Eqs. (2.15)-(2.17) are repeated until $|p^{n+1}-p^n|/\rho<\varepsilon$ (e.g., $\varepsilon=10^{-6}$) is satisfied in the whole domain.

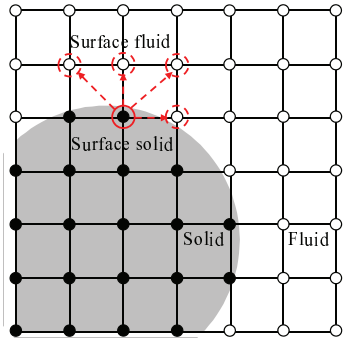

Figure 1: 2D sketch of the boundary condition for wetting.

The boundary condition for the function f_i is changed from [6] in order to introduce the wettability on walls. The half-way bounce back boundary condition [7] and the wetting boundary condition [5] are used for f_i. In the wetting boundary condition, the value of the order parameter at the solid wall is estimated by

$$\phi_{\text{wall}} = \sum_{i=1}^{N} \frac{\left[\phi_{\text{fluid}} - |\Delta x| \left(\frac{\gamma_{\text{wet}}}{\kappa_f}\right)\right]}{N}, \tag{2.18}$$

where subscript "wall" and "fluid" represent the solid and the fluid lattice points nearest to the solid surface, and N represents the total number of the nearest fluid lattice points to the solid lattice point (Fig. 1). In Eq. (2.18), κ_f is a constant parameter determining the width of the interface, and γ_{wet} is the wetting potential [8–13].

2.2 Computational setup and conditions

The computational domain is discretized into $L_x \times L_y \times L_z = 240 \times 120 \times 120$ cubic lattices (see Fig. 2). The gas channel with the width of $80\Delta x$, the height of $40\Delta x$ and the length of $240\Delta x$ is set at the top of the computational domain. The GDL with the width of $120\Delta x$, the height of $60\Delta x$ and the length of $240\Delta x$ is set under the separator. The porosity and the fiber diameter of the GDL are set to 78%, and $5\Delta x$, respectively. The rib is defined as the contact faces between separator and the GDL, and other area are set as solid point unrelated to calculation.

In our past study [1], the reconstructed GDL structure obtained by X-ray CT imaging shown in Fig. 3 was used, and its structural properties were validated compared with the experimental measurement of permeability. In this study, however, the Virtual Material Design [4] is applied to make the GDL structures because of its easiness to change the parameters such as fiber diameter, porosity, and anisotropy for their optimization. Among the various types of GDLs, a carbon paper is chosen and the fiber diameter, porosity, and thickness is used as setting values. That is, the GDL is assumed to be isotropic in the x and y directions and fibers are filled until the porosity becomes the setting value. After

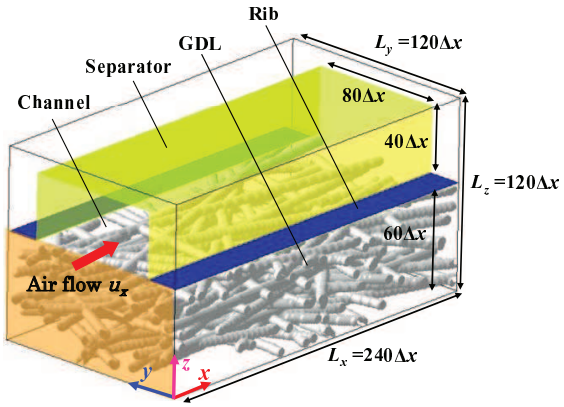

Figure 2: Computational setup.

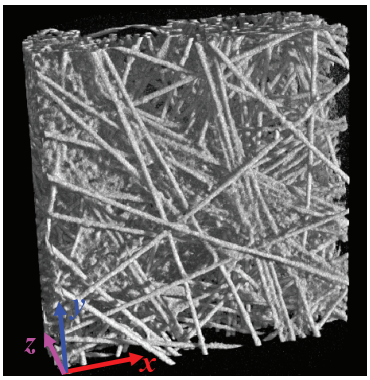

Figure 3: Reconstructed X-ray computed tomography image of GDL.

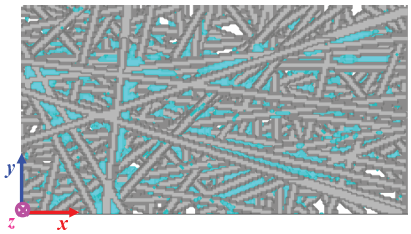

Figure 4: Simulated GDL structure (fiber and binder).

that, binder or water-repellent are filled to the curvature constant until filling fraction becomes the setting value (see Fig. 4). In order to verify the validity of the reconstructed structure, the permeability were calculated and compared with experimental results.

For the initial condition, the gas channel is filled with air and the GDL is filled with the mist of $\phi = 0.30$. The air flows into the gas channel with the velocity $u_x = 5.0 \times 10^{-4}$ from the inlet ($x = 0$). The liquid water is assumed to be produced at the bottom of the GDL according to the current density of the PFEC. Its velocity u_z can be obtained by using the following equations:

$$\sum_{n=1}^{N_r} \rho_L u_z = \frac{1}{2} \times \frac{1}{96500} \times \frac{18}{1000} \times I \times \frac{S}{\rho_0 c L^2}, \tag{2.19}$$

where ρ_L is the liquid density, u_z is the water inlet velocity in the z direction, 96500C/mol is the Faraday constant, 18 is the molecular weight of water, 1/2 is the number of water moles produced per electron, and I and S are the current density and the bottom area of

the PEFC. Also, ρ_0, c, and L are the reference quantities for density, velocity, and length, respectively, which are used for defining dimensionless variables in the computation. It is noted that the liquid water is not produced at the entire bottom of the GDL, but it is produced at 10% of lattice points ($n = N_r$) on the bottom using random numbers. That is, it is assumed that the water flows into the GDL from specific large pores in the catalyst layer. For the outlet boundary condition, constant gradient boundary condition is applied to pressure and no gradient boundary condition is applied to other physical quantities at the outlet of the channel ($x=L_x$). The periodic boundary condition is applied in the y direction, and the non-slip and the wetting boundary condition are used at the top and the bottom walls in the z direction.

The density and viscosity ratios of the air to the water are $\rho_L/\rho_G = 854$, and $\mu_L/\mu_G = 48.6$, respectively. The parameter values are $a = 1$, $b = 1$, $T = 0.29$, and it follows that the maximum and minimum values of the order parameter are $\phi_{max} = 0.40$ and $\phi_{min} = 0.26$. The cut-off values of the order parameter are ϕ_L=0.38 and ϕ_G=0.27. The other parameters are fixed at $\kappa_f = 0.05(\Delta x)^2$, $\tau_f = 1$, $\tau_g = 1$, $C = 0$, $g = 9.8\times10^{-14}$, where τ_f and τ_g are the non-dimensional relaxation times, C is the mobility parameter, and g is the gravity force.

3 Results

In our past study [14], the visualization experiment and the numerical simulation of water droplet transport in the gas channels were compared. There are several experimental approaches to visualize the water distribution in the PEFC such as the neutron imaging [15], Magnetic resonance imaging [16], and the X-ray computed tomography technique [17–19]. In this study, the in-situ micro focus X-ray computed tomography in operating condition is compared with numerical simulations of the water distribution in the GDL. The mechanism of water transport in the PEFC depends on the channel geometry, gas velocities, temperature, wettabilities, etc. In particular, the effects of wettability of the GDL and the channel wall on the water transport are investigated.

3.1 Comparison with experimental result

The numerical results conducted at a current density 1.0A/cm^2 are shown in Fig. 5. The contact angles of the GDL and the channel wall are 75° and 60°, respectively. Fig. 5 shows the time evolutions of water distribution at three different non-dimensional times $t^*(= L_x t/u_x)$. As shown in Fig. 5, the liquid water gathers in small pores among the hydrophilic fibers and stays under the rib which is more hydrophilic than the carbon fibers.

Experimental results, obtained by the micro focus X-ray computed tomography system, are arranged as follows. Fig. 6 shows a fuel cell reconstructed by the X-ray computed tomography. The operating temperature is 305K and the current density is 0.3A/cm^2. The GDL is made of the Toray TGP-H060 without hydrophobic treatment, and its wettability is weakly hydrophilic. Fig. 7 shows the procedure of image processing of $a-a'$

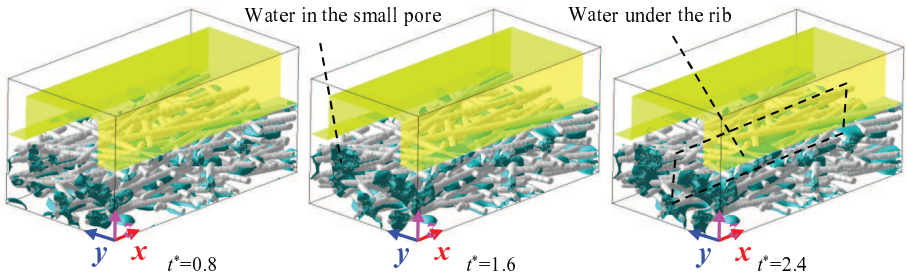

Figure 5: Time evolution of water distribution ($\theta_{\mathrm{GDL}}=75°$, $\theta_{\mathrm{channel}}=60°$).

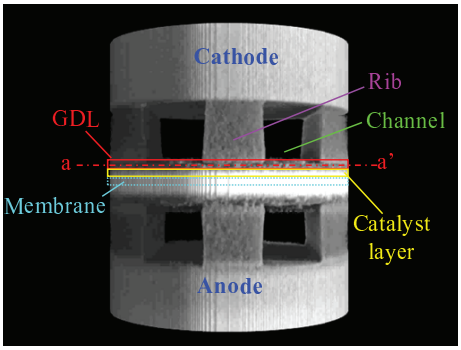

Figure 6: Three dimensional X-ray CT image of PEFC.

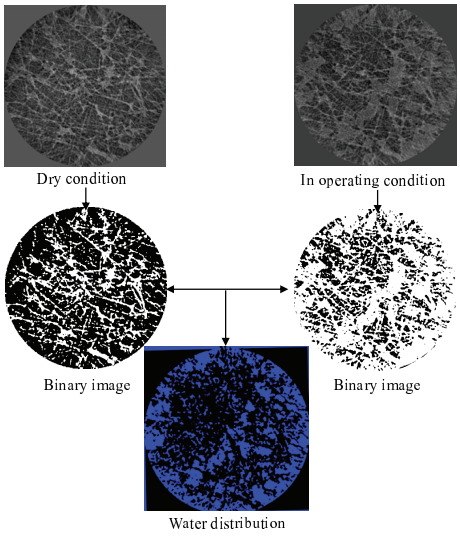

Figure 7: Procedure of image processing.

cross section in Fig. 6. The spatial resolution of X-ray computed tomography is set to 2μm. In Fig. 7, one is in dry condition, which is before operation, and another is in an operating condition. The dry condition image is converted into a binary image of pores and fibers, and the in-operation image is converted into a binary image of pores and the mixture of waters and fibers. By calculating the difference between the two images, the water distribution in the GDL can be obtained.

As seen in Figs. 5 and 7, the simulation and the experiment show agreement on the point that the water accumulates in small pores among the fibers more stable than in large pores. Fig. 8 shows the three-dimensional water distribution obtained by the image processing of X-ray computed tomography images. As seen in Figs. 5 and 8, a large amount of water stays under the rib.

Fig. 9 shows the distribution of water saturation in the GDL. The water saturation is defined by the averaged ratio of water volume to the pore volume. In the figure, the

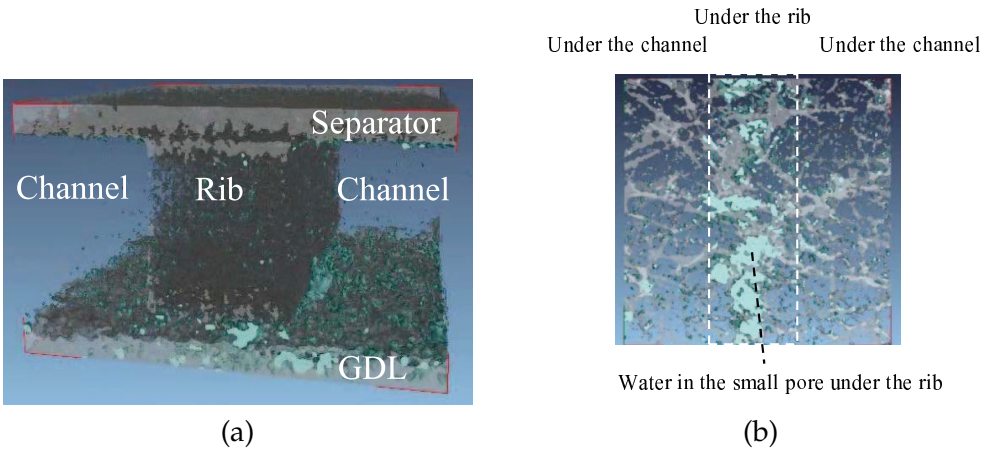

Figure 8: Three dimensional water distribution in the GDL reconstructed by X-ray CT imaging. (a) In the GDL and channel; (b) in the GDL near the channel and rib.

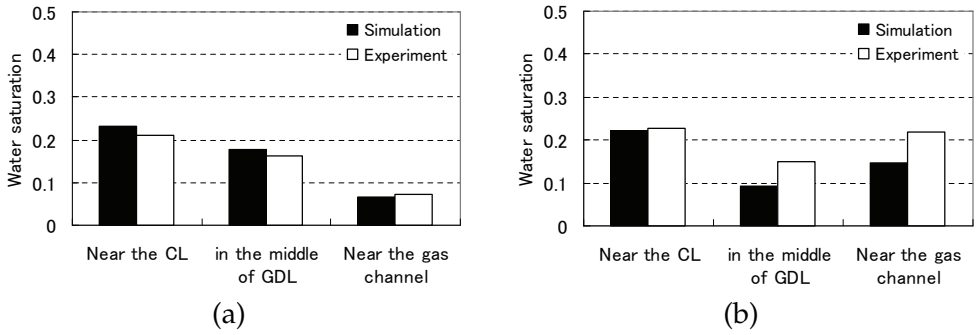

Figure 9: Comparison between simulation and experiment. (a) Under the channel; (b) under the rib.

water saturation near the catalyst layer, in the middle of the GDL, and near the channel is compared with the experiment. It is seen that the simulation results qualitatively agree with the experimental results both under the channel and under the rib. It is also found that more water stays near the catalyst layer than near the channel (see Fig. 9(a)), and more water stays under the rib than under the channel.

3.2 The effect of wettabilities of the GDL and the channel wall

Firstly, in order to investigate the effect of wettability of the GDL, simulations are carried out with the hydrophobic and hydrophilic GDLs. The contact angles of the hydrophobic and the hydrophilic cases are 120° and 75°, respectively, and the contact angle of the channel wall is set at 60° for the both cases. The results of the hydrophobic case are shown in Fig. 10, and those of the hydrophilic case have already been shown in Fig. 5. As shown in Fig. 10, the liquid water gathers in large pores in the hydrophobic GDL, and the liquid water under the rib is increased after the liquid water path connects from the

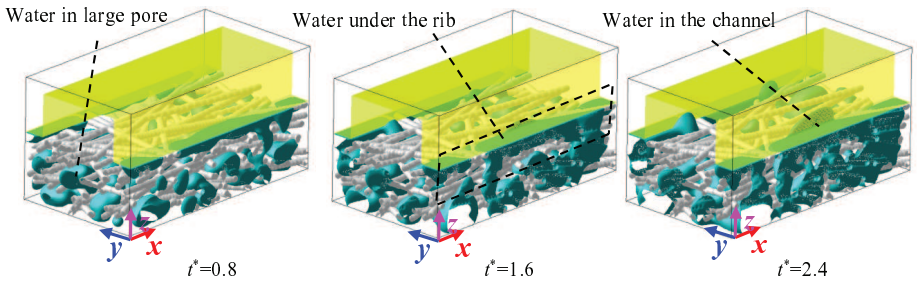

Figure 10: Time evolution of water distribution ($\theta_{\mathrm{GDL}}=120^\circ$, $\theta_{\mathrm{channel}}=60^\circ$).

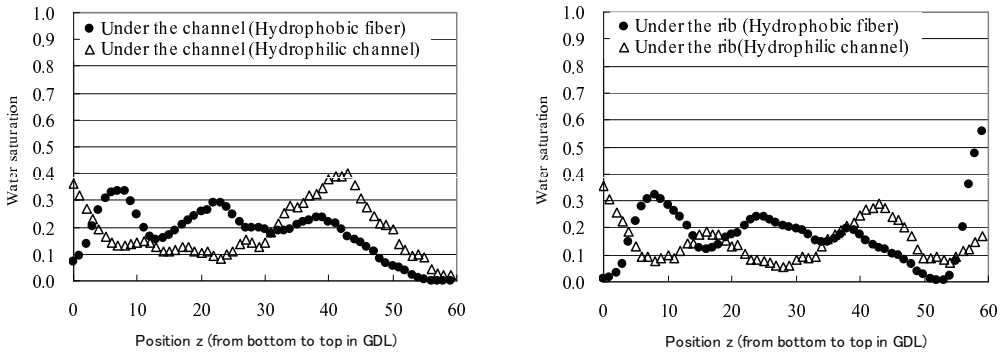

(a) (b)

Figure 11: Water saturation distribution ($\theta_{\mathrm{channel}}=60^\circ$). (a) Under the channel; (b) under the rib.

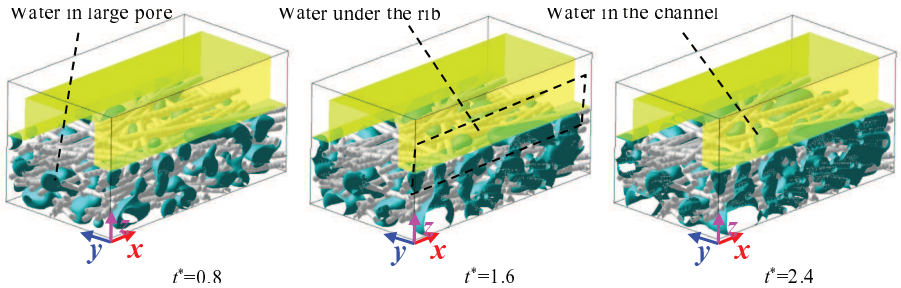

Figure 12: Time evolution of water distribution ($\theta_{\mathrm{GDL}}=120^\circ$, $\theta_{\mathrm{channel}}=120^\circ$).

bottom of the GDL to the rib. It is also found that the accumulated water under the rib is discharged along the hydrophilic channel wall.

Figs. 11(a) and 11(b) show the water saturation distribution in the hydrophobic and the hydrophilic GDL at the same saturation level in the GDL. The water saturation is defined by the averaged ratio of water volume to the pore volume in the $x-y$ plane at $t^*=0.8$. Fig. 11(a) shows the water saturation distribution under the channel in the z direction. On the other hand, Fig. 11(b) shows the water saturation distribution under the rib. It is seen that the water saturation distribution in the hydrophobic GDL is dif-

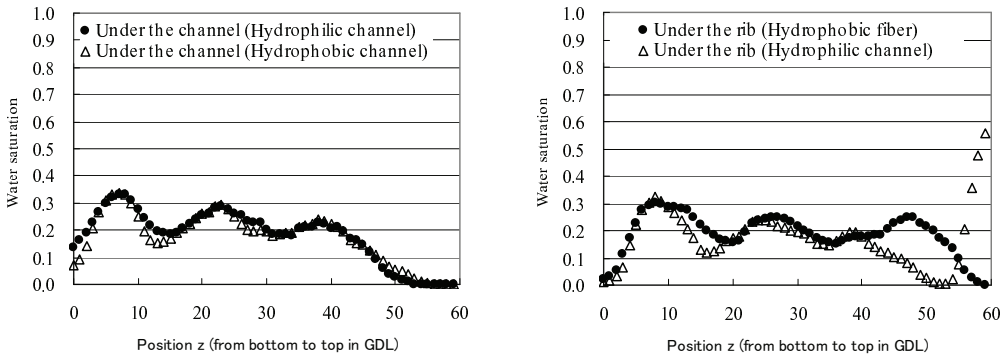

(a) (b)

Figure 13: Water saturation distribution ($\theta_{\rm GDL}=120^\circ$). (a) Under the channel; (b) under the rib.

ferent from that in the hydrophilic GDL, because the water stays in large pores in the hydrophobic GDL, but it remains in small pores in the hydrophilic GDL. Furthermore, it is found that the water saturation just under the rib, which is more hydrophilic than the GDL, becomes larger than that under the channel in both the hydrophobic and the hydrophilic GDL.

Secondly, in order to investigate the effect of wettability of the channel wall, the contact angle of the channel wall is changed to 120°. The contact angle of the GDL is set at 120°. The result is shown in Fig. 12. In both cases of the hydrophilic channel (Fig. 10) and the hydrophobic channel (Fig. 12), the water passes through large pores in the GDL and the liquid water under the rib diminishes due to the change in the wettability of the channel. Figs. 13(a) and 13(b) show the water saturation distribution in the GDL at the same saturation level. As seen from these figures, it is found that the liquid water under the rib can be diminished at low water saturation (see $t^*=0.8$ in Fig. 12) by changing the wettability of the channel wall from hydrophilic to hydrophobic.

4 Conclusions

The two-phase lattice Boltzmann method for high density ratio proposed by Inamuro [6], the boundary condition for wettability [5], and the half-way bounce back boundary condition [7] have been applied to simulations of the water transport from the GDL to the gas channel. Numerical results are compared with the X-ray computed tomography images, and they agree qualitatively. From the numerical investigations of the effect of wettabilities of the GDL and the channel wall on the water transport from the GDL to the gas channel, it is found that the liquid water passes through small pores in the hydrophilic GDL and large pores in the hydrophobic GDL. It is also found that more water stays under the rib than under the channel and the water under the rib can be diminished by changing the wettability of the channel wall from hydrophilic to hydrophobic. In a future

study, in order to find out the optimal condition for the PEFC, the effect of the porosity and the pore size distribution of the GDL, the channel geometry, the inlet gas velocity and the humidity on the water transport in the PEFC will be investigated. Furthermore, phase changes such as condensation by cooling water and evaporation near the catalyst layer should be considered.

References

[1] T. Koido, T. Furusawa, and K. Moriyama, An approach to modeling two-phase transport in the gas diffusion layer of a proton exchange membrane fuel cell, J. Power. Sources., 175 (2008), 127–136.
[2] X. G. Yang, F. Y. Zhang, A. L. Lubawy, and C. Y. Wang, Visualization of liquid water transport in a PEFC, Electrochem. Solid. State. Lett., 7(11) (2004), A408–A411.
[3] F. Y. Zhang, X. G. Yang, and C. Y. Wang, Liquid water removal from a polymer electrolyte fuel cell, J. Electrochem. Soc., 153(2) (2006), A225–A232.
[4] V. P. Schulz, J. Becker, A. Wiegmann, P. P. Mukherjee, and C. Y. Wang, Modeling of two-phase behavior in the gas diffusion medium of PEFCs in full morphology approach, J. Electrochem. Soc., 154 (2007), B419–B426.
[5] X. D. Niu, T. Munekata, S. Hyodo, and K. Suga, An investigation of water-gas transport process in the gas-diffusion-layer of a PEM fuel cell by a multiphase multiple-relaxation-time lattice Boltzmann model, J. Power. Sources., 172 (2007), 542–552.
[6] T. Inamuro, T. Ogata, S. Tajima, and N. Konishi, A lattice Boltzmann method for incompressible two-phase flows with large density differences, J. Comput. Phys., 198 (2004), 628–644.
[7] X. He, Q. Zou, L. -S. Luo, and M. Dembo, Analytic solutions of simple flows and analysis of nonslip boundary conditions for the lattice Boltzmann BGK model, J. Stat. Phys., 87 (1997), 115–136.
[8] A. J. Briant, P. Paatzacos, and J. M. Yeomans, Lattice Boltzmann simulations of contact line motion in a liquid-gas system, Philos. Trans. Roy. Soc. London. A., 360 (2002), 485–495.
[9] A. J. Briant, A. J. Wagner, and J. M. Yeomans, Lattice Boltzmann simulations of contact line motion: I. liquid-gas systems, Phys. Rev. E., 69 (2004), 031602.
[10] A. J. Briant, and J. M. Yeomans, Lattice Boltzmann simulations of contact line motion: II. binary fluids, Phys. Rev. E., 69 (2004), 031603.
[11] J. W. Cahn, and J. E. Hilliard, Free energy of a nonuniform system I. interfacial free energy, J. Chem. Phys., 28 (1958), 258–267.
[12] J. W. Cahn, Critical point weting, J. Chem. Phys., (1977), 3667–3672.
[13] K. Kobayashi, T. Inamuro, and F. Ogino, Numerical simulation of advancing interface in a micro heterogeneous channel by the lattice Boltzmann method, J. Chem. Eng. Jpn., 39 (2006), 257–266.
[14] K. Moriyama, and T. Inamuro, Numerical simulations of water droplet transport in microchannels using the two-phase lattice Boltzmann method, Trans. Jpn. Soc. Mech. Eng. Ser. B., (2009), 09-0356.
[15] D. S. Hussey, D. L. Jacobson, M. Arif, J. P. Owejan, J. J. Gagliardo, and T. A. Trabold, Neutron imagings of the through-plane water distribution of an operating PEM fuel cell, J. Power. Sources., 172(1) (2007), 225–228.
[16] K. Teranishi, S. Tsushima, and S. Hirai, Analysis of water transport in PEFCs by magnetic resonance imaging measurement, J. Electrochem. Soc., 153 (2006), A664–668.

[17] P. K. Sinha, P. Halleck, and C. Y. Wang, Quantification of liquid water saturation in a PEM fuel cell diffusion medium using *X*-ray microtomography, Electrochem. Solid. State. Lett., 9 (2006), A344–348.
[18] S. R. Stock, Microtomography of materials, Int. Mater. Rev., 44 (1999), 141–169.
[19] D. Wildenschild, J. W. Hopmans, C. M. P. Vaz, M. L. Rivers, and D. Rikard, Using *X*-ray computed tomography in hydrology: systems, resolutions, and limitations, J. Hydrol., 267(3-4) (2002), 285–297.